PHYSICAL REVIEW D VOLUME 50, NUMBER 9 1 NOVEMBER 1994

Measurement of $\bar{p}p$ single diffraction dissociation at $\sqrt{s} = 546$ and 1800 GeV

F. Abe,[12] M. Albrow,[6] D. Amidei,[15] C. Anway-Wiese,[3] G. Apollinari,[23] M. Atac,[6] P. Auchincloss,[22] P. Azzi,[17] N. Bacchetta,[16] A. R. Baden,[8] W. Badgett,[15] M. W. Bailey,[21] A. Bamberger,[6,*] P. de Barbaro,[22] A. Barbaro-Galtieri,[13] V. E. Barnes,[21] B. A. Barnett,[11] G. Bauer,[14] T. Baumann,[8] F. Bedeschi,[20] S. Behrends,[2] S. Belforte,[20] G. Bellettini,[20] J. Bellinger,[28] D. Benjamin,[27] J. Benlloch,[14] J. Bensinger,[2] A. Beretvas,[6] J. P. Berge,[6] S. Bertolucci,[7] K. Biery,[10] S. Bhadra,[9] M. Binkley,[6] D. Bisello,[17] R. Blair,[1] C. Blocker,[2] A. Bodek,[22] V. Bolognesi,[20] A. W. Booth,[6] C. Boswell,[11] G. Brandenburg,[8] D. Brown,[8] E. Buckley-Geer,[6] H. S. Budd,[22] G. Busetto,[17] A. Byon-Wagner,[6] K. L. Byrum,[1] C. Campagnari,[6] M. Campbell,[15] A. Caner,[6] R. Carey,[8] W. Carithers,[13] D. Carlsmith,[28] J. T. Carroll,[6] R. Cashmore,[6,*] A. Castro,[17] Y. Cen,[18] F. Cervelli,[20] K. Chadwick,[6] J. Chapman,[15] T. J. Chapin,[23] G. Chiarelli,[7] W. Chinowsky,[13] S. Cihangir,[6] A. G. Clark,[6] M. Cobal, [20] D. Connor,[18] M. Contreras,[4] J. Cooper,[6] M. Cordelli,[7] D. Crane,[6] J. D. Cunningham,[2] C. Day,[6] F. DeJongh,[6] S. Dell'Agnello,[20] M. Dell'Orso,[20] L. Demortier,[23] B. Denby,[6] P. F. Derwent,[15] T. Devlin,[24] M. Dickson,[22] R. B. Drucker,[13] A. Dunn,[15] K. Einsweiler,[13] J. E. Elias,[6] R. Ely,[13] S. Eno,[4] S. Errede,[9] A. Etchegoyen,[6,*] B. Farhat,[14] M. Frautschi,[16] G. J. Feldman,[8] B. Flaugher,[6] G. W. Foster,[6] M. Franklin,[8] J. Freeman,[6] T. Fuess,[6] Y. Fukui,[12] A. F. Garfinkel,[21] A. Gauthier,[9] S. Geer,[6] D. W. Gerdes,[15] P. Giannetti,[20] N. Giokaris,[23] P. Giromini,[7] L. Gladney,[18] M. Gold,[16] J. Gonzalez,[18] K. Goulianos,[23] H. Grassmann,[17] G. M. Grieco,[20] R. Grindley,[10] C. Grosso-Pilcher,[4] C. Haber,[13] S. R. Hahn,[6] R. Handler,[28] K. Hara,[26] B. Harral,[18] R. M. Harris,[6] S. A. Hauger,[5] J. Hauser,[3] C. Hawk,[24] T. Hessing,[25] R. Hollebeek,[18] L. Holloway,[9] A. Hölscher,[10] S. Hong,[15] G. Houk,[18] P. Hu,[19] B. Hubbard,[13] B. T. Huffman,[19] R. Hughes,[22] P. Hurst,[8] J. Huth,[6] J. Hylen,[6] M. Incagli,[20] T. Ino,[26] H. Iso,[26] C. P. Jessop,[8] R. P. Johnson,[6] U. Joshi,[6] R. W. Kadel,[13] T. Kamon,[25] S. Kanda,[26] D. A. Kardelis,[9] I. Karliner,[9] E. Kearns,[8] L. Keeble,[25] R. Kephart,[6] P. Kesten,[2] R. M. Keup,[9] H. Keutelian,[6] D. Kim,[6] S. B. Kim,[15] S. H. Kim,[26] Y. K. Kim,[13] L. Kirsch,[2] K. Kondo,[26] J. Konigsberg,[8] K. Kordas,[10] E. Kovacs,[6] M. Krasberg,[15] S. E. Kuhlmann,[1] E. Kuns,[24] A. T. Laasanen,[21] S. Lammel,[3] J. I. Lamoureux,[28] S. Leone,[20] J. D. Lewis,[6] W. Li,[1] P. Limon,[6] M. Lindgren,[3] T. M. Liss,[9] N. Lockyer,[18] M. Loreti,[17] E. H. Low,[18] D. Lucchesi,[20] C. B. Luchini,[9] P. Lukens,[6] P. Maas,[28] K. Maeshima,[6] M. Mangano,[20] J. P. Marriner,[6] M. Mariotti,[20] R. Markeloff,[28] L. A. Markosky,[28] J. A. J. Matthews,[16] R. Mattingly,[2] P. McIntyre,[25] A. Menzione,[20] E. Meschi,[20] T. Meyer,[25] S. Mikamo,[12] M. Miller,[4] T. Mimashi,[26] S. Miscetti,[7] M. Mishina,[12] S. Miyashita,[26] Y. Morita,[26] S. Moulding,[23] J. Mueller,[24] A. Mukherjee,[6] T. Muller,[3] L. F. Nakae,[2] I. Nakano,[26] C. Nelson,[6] D. Neuberger,[3] C. Newman-Holmes,[6] J. S. T. Ng,[8] M. Ninomiya,[26] L. Nodulman,[1] S. Ogawa,[26] R. Paoletti,[20] V. Papadimitriou,[6] A. Para,[6] E. Pare,[8] S. Park,[6] J. Patrick,[6] G. Pauletta,[20] L. Pescara,[17] T. J. Phillips,[5] A. G. Piacentino,[20] R. Plunkett,[6] L. Pondrom,[28] J. Proudfoot,[1] F. Ptohos,[8] G. Punzi,[20] D. Quarrie,[6] K. Ragan,[10] G. Redlinger,[4] J. Rhoades,[28] M. Roach,[27] F. Rimondi,[6,*] L. Ristori,[20] W. J. Robertson,[5] T. Rodrigo,[6] T. Rohaly,[18] A. Roodman,[4] W. K. Sakumoto,[22] A. Sansoni,[7] R. D. Sard,[9] A. Savoy-Navarro,[6] V. Scarpine,[9] P. Schlabach,[8] E. E. Schmidt,[6] O. Schneider,[13] M. H. Schub,[21] R. Schwitters,[8] G. Sciacca,[20] A. Scribano,[20] S. Segler,[6] S. Seidel,[16] Y. Seiya,[26] G. Sganos,[10] N. M. Shaw,[21] M. Sheaff,[28] M. Shochet,[4] J. Siegrist,[13] A. Sill,[22] P. Sinervo,[10] J. Skarha,[11] K. Sliwa,[27] D. A. Smith,[20] F. D. Snider,[11] L. Song,[6] T. Song,[15] M. Spahn,[13] P. Sphicas,[14] A. Spies,[11] R. St. Denis,[8] L. Stanco,[17] A. Stefanini,[20] G. Sullivan,[4] K. Sumorok,[14] R. L. Swartz, Jr.,[9] M. Takano,[26] K. Takikawa,[26] S. Tarem,[2] F. Tartarelli,[20] S. Tether,[14] D. Theriot,[6] M. Timko,[27] P. Tipton,[22] S. Tkaczyk,[6] A. Tollestrup,[6] J. Tonnison,[21] W. Trischuk,[8] Y. Tsay,[4] J. Tseng,[11] N. Turini,[20] F. Ukegawa,[26] D. Underwood,[1] S. Vejcik III,[15] R. Vidal,[6] R. G. Wagner,[1] R. L. Wagner,[6] N. Wainer,[6] R. C. Walker,[22] J. Walsh,[18] A. Warburton,[10] G. Watts,[22] T. Watts,[24] R. Webb,[25] C. Wendt,[28] H. Wenzel,[20] W. C. Wester III,[13] T. Westhusing,[9] S. N. White,[23] A. B. Wicklund,[1] E. Wicklund,[6] H. H. Williams,[18] B. L. Winer,[22] J. Wolinski,[25] D. Y. Wu,[15] X. Wu,[20] J. Wyss,[17] A. Yagil,[6] K. Yasuoka,[26] Y. Ye,[10] G. P. Yeh,[6] J. Yoh,[6] M. Yokoyama,[26] J. C. Yun,[6] A. Zanetti,[20] F. Zetti,[20] S. Zhang,[15] W. Zhang,[18] and S. Zucchelli[6,*]

(CDF Collaboration)

[1] *Argonne National Laboratory, Argonne, Illinois 60439*
[2] *Brandeis University, Waltham, Massachusetts 02254*
[3] *University of California at Los Angeles, Los Angeles, California 90024*
[4] *University of Chicago, Chicago, Illinois 60637*
[5] *Duke University, Durham, North Carolina 27706*
[6] *Fermi National Accelerator Laboratory, Batavia, Illinois 60510*
[7] *Laboratori Nazionali di Frascati, Istituto Nazionale di Fisica Nucleare, Frascati, Italy*
[8] *Harvard University, Cambridge, Massachusetts 02138*
[9] *University of Illinois, Urbana, Illinois 61801*
[10] *Institute of Particle Physics, McGill University, Montreal, and University of Toronto, Toronto, Canada*
[11] *The Johns Hopkins University, Baltimore, Maryland 21218*

---

[*] Visitor.

0556-2821/94/50(9)/5535(15)/$06.00

[12] *National Laboratory for High Energy Physics (KEK), Japan*
[13] *Lawrence Berkeley Laboratory, Berkeley, California 94720*
[14] *Massachusetts Institute of Technology, Cambridge, Massachusetts 02139*
[15] *University of Michigan, Ann Arbor, Michigan 48109*
[16] *University of New Mexico, Albuquerque, New Mexico 87131*
[17] *Universita di Padova, Instituto Nazionale di Fisica Nucleare, Sezione di Padova, I-35131 Padova, Italy*
[18] *University of Pennsylvania, Philadelphia, Pennsylvania 19104*
[19] *University of Pittsburgh, Pittsburgh, Pennsylvania 15260*
[20] *Istituto Nazionale di Fisica Nucleare, University and Scuola Normale Superiore of Pisa, I-56100 Pisa, Italy*
[21] *Purdue University, West Lafayette, Indiana 47907*
[22] *University of Rochester, Rochester, New York, 15627*
[23] *Rockefeller University, New York, New York 10021*
[24] *Rutgers University, Piscataway, New Jersey 08854*
[25] *Texas A&M University, College Station, Texas 77843*
[26] *University of Tsukuba, Tsukuba, Ibaraki 305, Japan*
[27] *Tufts University, Medford, Massachusetts 02155*
[28] *University of Wisconsin, Madison, Wisconsin 53706*

(Received 5 August 1993)

We report a measurement of the diffraction dissociation differential cross section $d^2\sigma_{\rm SD}/dM^2dt$ for $\bar{p}p \to \bar{p}X$ at $\sqrt{s} = 546$ and 1800 GeV, $M^2/s < 0.2$ and $0 \leq -t \leq 0.4$ GeV^2. Our results are compared to theoretical predictions and to extrapolations from experimental results at lower energies.

PACS number(s): 13.85.Hd, 12.40.Nn

I. INTRODUCTION

As part of a measurement of the $\bar{p}p$ total cross sections at the Fermilab Tevatron collider at c.m. system (c.m.s.) energies $\sqrt{s} = 546$ and 1800 GeV, we have studied proton diffraction dissociation, $\bar{p}p \to \bar{p}X$, by detecting the recoil antiproton and a large fraction of the particles of the system X. The same experimental apparatus was also used for the simultaneous measurement of elastic scattering and of the total cross sections, which are reported in the preceding [1] and following [2] papers.

Although single diffraction dissociation has its roots in the basic principles of quantum mechanics [3], it is still lacking basic understanding in terms of QCD. As discussed extensively in textbooks [4] and review articles [5–7], its theoretical description is based on Regge phenomenology, which ascribes single diffraction dissociation to the exchange of the Pomeron, a Regge trajectory that carries the quantum numbers of the vacuum.

Previous experiments found that the cross section $d^2\sigma_{\rm SD}/dM^2$ has a weak s dependence and varies approximately as e^{bt}/M^2, where M is the mass of the system X. This experiment, with its long lever arms in s and M^2 coupled with good mass resolution, provides a more precise determination of the s and M^2 dependence of the cross section, allowing for interesting comparisons with theoretical models and with the s dependence of the elastic and total cross sections.

As described in Sec. II, the experiment employed a magnetic spectrometer that measured the recoil antiproton momentum with good resolution, $\Delta p/p \approx 10^{-3}$, over large acceptance, $M^2/s \leq 0.2$ and $|t| \leq 0.4$ GeV^2, at two widely spaced high energies, $\sqrt{s} = 546$ and 1800 GeV. The measurement benefited from the use of the powerful Collider Detector at Fermilab (CDF) tracking system in studying the multiparticle state X. In Sec. III, we show that these experimental features provided a practically background-free sample of single diffraction events. In Sec. IV the multiplicity and pseudorapidity distributions from our data are compared to the predictions of a Monte Carlo simulation employing a simple decay mechanism for the excited masses. Sections V and VI, describe how the good resolution and redundancy in this measurement, combined with the available large kinematic range, allowed the determination of the M^2, t, and s dependence with high accuracy and, contrary to all previous experiments, without the need for any phenomenological assumption. In Sec. VI, our model-independent results are used to test the predictions of Pomeron exchange models, which until now were almost exclusively restricted to the more accurate studies of elastic scattering and total cross section. Previous experiments at the CERN Intersecting Storage Rings (ISR), Super Proton Synchrotron (SPS), and Fermilab often reported significant differences in single diffraction dissociation cross section values, which were mostly due to different phenomenological interpretations of the data. In Sec. VI C, old data at $\sqrt{s} = 20$ GeV are reanalyzed to provide consistent $\sigma_{\rm SD}$ data over a wide energy range. In Secs. VI C and VI D, we compare our data to results of some previous experiments, using their phenomenological assumptions; we show that, while the data are consistent, the assumptions are not always compatible with all the experimental evidence available in our experiment. Our conclusions are presented in Sec. VII.

II. EXPERIMENTAL METHOD

The recoil antiproton was observed by a magnetic spectrometer composed of two arms in the horizontal plane of the machine: arm 0 on the outside and arm 1 on the inside of the Tevatron beam orbit. In each arm, the outgoing $\bar{p}$ trajectory on the west side of the interaction region was measured at three different z points along the beam line by detectors $S3$, $S2$, and $S1$ placed inside beam pipe sections with variable aperture (Fig. 1 of [1]). Each detector consisted of four planes of drift chambers, a silicon detector and two trigger counters.

The charged particles from the proton fragmentation were observed by the tracking detectors $S4$, FTB, VTPC, FTF and $S5$ (Fig. 1 of [2]). The VTPC [8], a system of eight time projection chambers around the beam pipe, covered the pseudorapidity region $|\eta| < 3.5$. In addition, four telescopes of drift wire chambers, symmetrically placed on the west side (FTB,$S4$) and the east side (FTF,$S5$) of the interaction region, covered the region $3.8 < |\eta| < 6.7$. Each telescope was backed by time of flight (TOF) and trigger counters ($3.2 < |\eta| < 6.7$).

The trigger required a particle through detectors $S1$ and $S2$ in coincidence with at least one particle in the region $3.2 < \eta < 6.7$ on the proton fragmentation side. The recoil antiproton was deflected in the horizontal (x-z) plane by the Tevatron dipole and quadrupole magnets. Its momentum p and recoil angle θ were first calculated from the (x_1, y_1) and (x_2, y_2) positions measured by $S1$ and $S2$, using the well-known values of the machine lattice transfer matrices [1] and assuming $x = y = 0$ at $z = 0$. The projected position $(x_{3\ \mathrm{proj}}, y_{3\ \mathrm{proj}})$ in $S3$ was also evaluated and used in making fiducial cuts. For events passing the fiducial cuts, the recoil angle and momentum was then recalculated using also the (x_3, y_3) position.

The momentum resolution $\sigma_p(p)$ at $p_0 = \sqrt{s}/2$ was determined by reconstructing the antiproton momentum in a sample of elastic events. As shown in Fig. 1, the measured $\sigma_p(p_0)/p_0$ is about 0.14% (0.089%) at $\sqrt{s} = 546$ (1800) GeV and agrees with our spectrometer simulation, which accounts for the detector resolution and the beam profile and angular spread at the interaction point (see Appendix D of [1]). For $p < p_0$, the simulation shows that at $\sqrt{s} = 546$, where data were taken with the low β quadrupoles almost at full power $\sigma_p(p) = 0.4(p/p_0)[1 - 4(p_0 - p)/p_0]$ GeV. In the high β runs at $\sqrt{s} = 1800$, $\sigma_p(p) = 0.8(p/p_0)$ GeV. The momentum and angle of the recoil antiproton were used to calculate the Feynman scaling variable $x = p/p_0$, the system X mass $M^2 = (1 - x)s$, and the four-momentum transfer $t = -m_p^2(1 - x)^2/x - 2p_0^2 x(1 - \cos\theta)$, where m_p is the proton mass.

The simulated acceptance $A(x, t)$ of the recoil spectrometer is shown in Fig. 2. Given a functional form for $d^2\sigma/dM^2dt$ (see Sec. V), we fitted to the data the product $d^2\sigma/dM^2dt\, A(x, t)E(M^2)$ in the region where $A(x, t)$ is larger than 0.02; $E(M^2)$ is the efficiency for triggering and reconstructing the vertex for a given M. The total single diffraction cross section was obtained by integrating $d^2\sigma_{\mathrm{SD}}/dM^2dt$ over the full momentum transfer in the diffraction region [6,7] 1.4 $\mathrm{GeV}^2 < M^2 < 0.15s$.

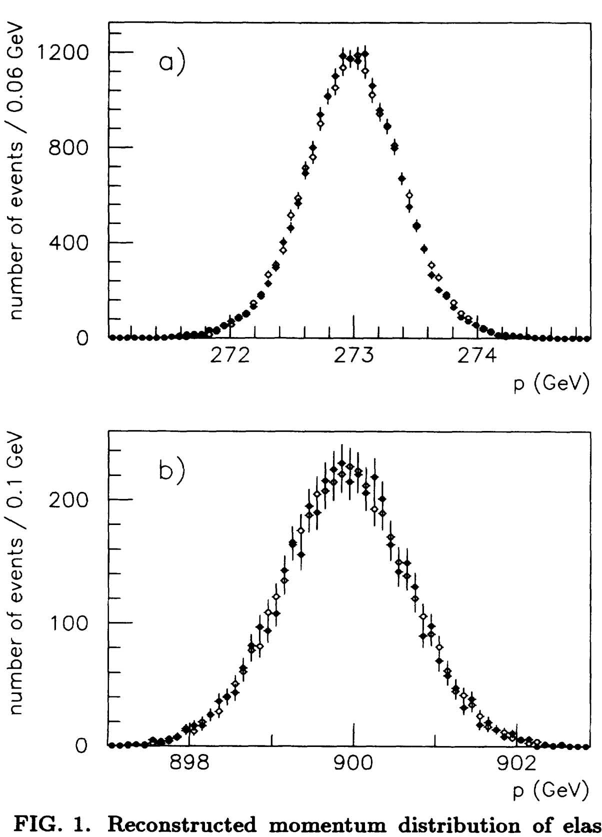

FIG. 1. Reconstructed momentum distribution of elastic events at (a) $\sqrt{s} = 546$ and (b) $\sqrt{s} = 1800$: (●) data; (○) simulation. The corresponding diffractive mass resolution is $\delta M^2 = (21\ \mathrm{GeV})^2$ and $(54\ \mathrm{GeV})^2$ at $\sqrt{s} = 546$ and 1800, respectively.

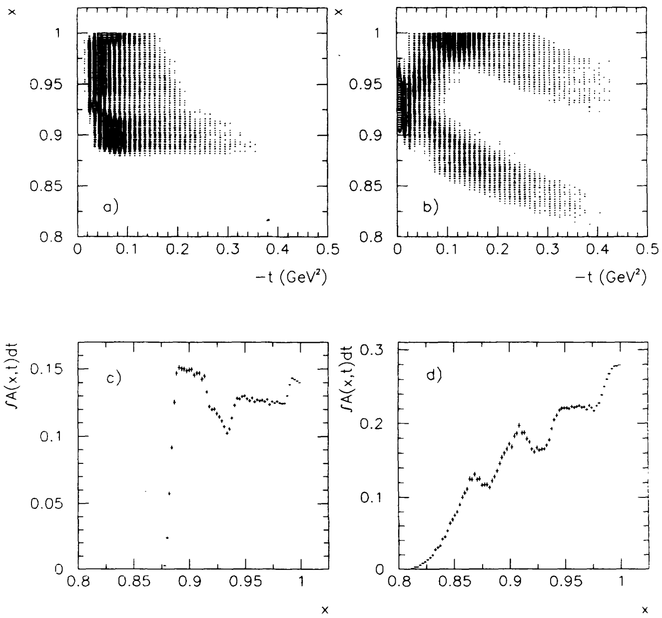

FIG. 2. Spectrometer acceptance $A(x, t)$ at (a) $\sqrt{s} = 546$ and (b) $\sqrt{s} = 1800$. Integrated acceptance $\int_0^{0.5} A(x, |t|)d|t|$ at (c) $\sqrt{s} = 546$ and (d) $\sqrt{s} = 1800$.

TABLE I. Analysis event flow.

	$\sqrt{s} = 546$ No. of events	1st run at $\sqrt{s} = 1800$ No. of events	2nd run at $\sqrt{s} = 1800$ No. of events
Triggers	15 272	16 303	57 177
TOF FILTER	13 129	8 851	15 794
VTPC FILTER	12 683	7 813	13 777
HITS CUT	12 058	6 884	10 561
$S1^*S2$ TRACK CUT	10 462	6 093	9 192
FIDUCIAL CUT 1+2+3	5 374	1 417	3 194
VERTEX CUT	4 637	1 090	2 616
Background removal	4 637	1 070	2 616
$A(x,t) > 0.02$	4 604	1 065	2 606
Loss corrections			
VTPC+TOF FILTER	1.011 ± 0.004	1.019 ± 0.002	1.018 ± 0.008
Nuclear interactions	1.024 ± 0.002	1.024 ± 0.002	1.024 ± 0.002
Prescaling factor ×2	1.84×2	1.8×2	1×2

III. DATA REDUCTION

From a total of 15 272 events collected in one run at $\sqrt{s} = 546$ and 73 480 events in two different runs at $\sqrt{s} = 1800$, we selected 4604 and 3671 events, respectively (see Table I). Events were rejected when halo particles in time with the incoming beams were detected by our time of flight counters (TOF FILTER) or if the VTPC detected particle showers originating upstream of the interaction region (VTPC FILTER). The losses due to TOF and VTPC filters were evaluated and are listed in Table I. Events were further rejected if $S1$ and $S2$ in the triggering arm had more than one hit and $S1$ or $S2$ in the opposite arm had more than four hits (HITS CUT). Otherwise, multihit events (1% of the total) were retained. Events were not accepted if we were unable to reconstruct a track segment in the $S1$ or $S2$ detectors ($S1^*S2$ TRACK CUT). The last two requirements do not cause appreciable inefficiencies, as shown by the analysis of our elastic events [1].

In accordance with our elastic scattering analysis, in order to avoid edge effects, we removed events which lay within 0.05 cm of detector boundaries (FIDUCIAL CUT 1).

When the projection of the measured antiproton trajectory was within the $S3$ detectors, the differences between the measured (x_3, y_3) coordinates and the projected coordinates were required to be within three times the detector spatial resolution (FIDUCIAL CUT 2). Since the machine dipoles bend the recoil antiprotons towards the inside of the beam orbit, $S3$ is always hit when events trigger arm 0, while $S3$ can be missed by events triggering arm 1. Figure 3 shows scatter plots of x_2 versus x_3 for all the accepted events at $\sqrt{s} = 546$, for the events which also pass the fiducial cuts and for simulated events with all cuts. Negative values of x_2 correspond to $\bar{p}$'s detected in arm 1, while x_2 is positive if $\bar{p}$'s are detected in arm 0. Elastically scattered $\bar{p}$'s would cluster along the solid line in Fig. 3(a). For a given x_3,

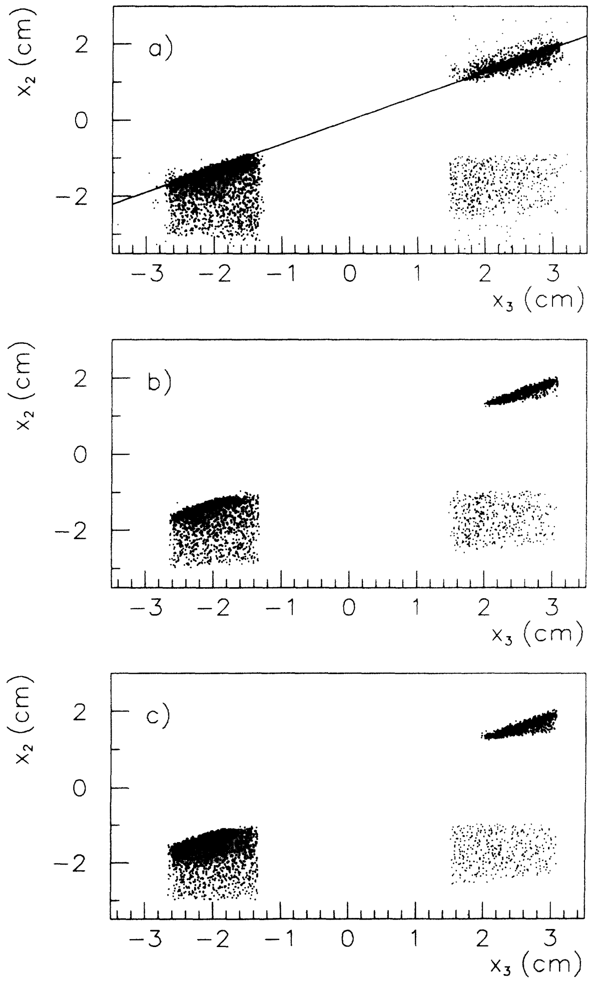

FIG. 3. Distribution of antiproton x_2 vs x_3 coordinates at $\sqrt{s} = 546$ (the $S2$ and $S3$ detectors are separated by a string of dipole magnets). (a) All accepted events; (b) events which also pass all fiducial cuts listed in Table I; (c) simulated events.

i.e., a given recoil angle θ, decreasing values of x_2 correspond to increasingly lower antiproton momenta and higher diffractive masses. In arm 0, events above the elastic scattering line are out of the spectrometer acceptance for particles originating at the interaction region and are due to antiprotons in the beam halo that have small θ angle but are sufficiently away from the beam center as to be detected. In arm 1, such halo particles can fake diffractive events. Similar plots for the first $\sqrt{s} = 1800$ run are shown in Fig. 4. Here, because of a different optical beam tune [1], halo particles fake diffractive events in arm 0, while they remain outside the acceptance in arm 1. To reduce the arm 0 halo background at $\sqrt{s} = 1800$, we limited the arm 0 acceptance in the x_2-x_3 plane as shown in Figs. 4(b) and 4(c). Similarly, to reduce the arm 1 background at $\sqrt{s} = 546$, we accepted only events in which $S3$ was also hit (FIDUCIAL CUT 3). The losses due to all fiducial cuts ($< 1\%$) were included in the acceptance calculation.

The requirements and cuts listed above removed most of the halo background. The residual halo contamination was evaluated by examining the distribution of (x_3-$x_{3\ \mathrm{proj}}$) after having applied all cuts listed in Table I except FIDUCIAL CUT 2. Figure 5(a) shows the distributions of (x_3-$x_{3\ \mathrm{proj}}$) in arm 1 for data and simulation at $\sqrt{s} = 546$. The background contribution was estimated to be $\ll 1\%$. Similar distributions are shown in Fig. 5(b) for arm 0 data from the first run at $\sqrt{s} = 1800$. The background is clearly visible as a shoulder on the right hand side of distribution. This background was attributed to beam halo particles. A good fraction of these particles could be tagged, as they were also observed by the $S6$ and $S7$ detectors of the elastic scattering spectrometer upstream of the interaction region. The distribution of (x_3-$x_{3\ \mathrm{proj}}$) for the tagged halo events is shown in Fig. 5(b), normalized to the region (x_3-$x_{3\ \mathrm{proj}}$) > 0.2 cm where no good events are expected from the simulation. From this distribution, the background contamination within

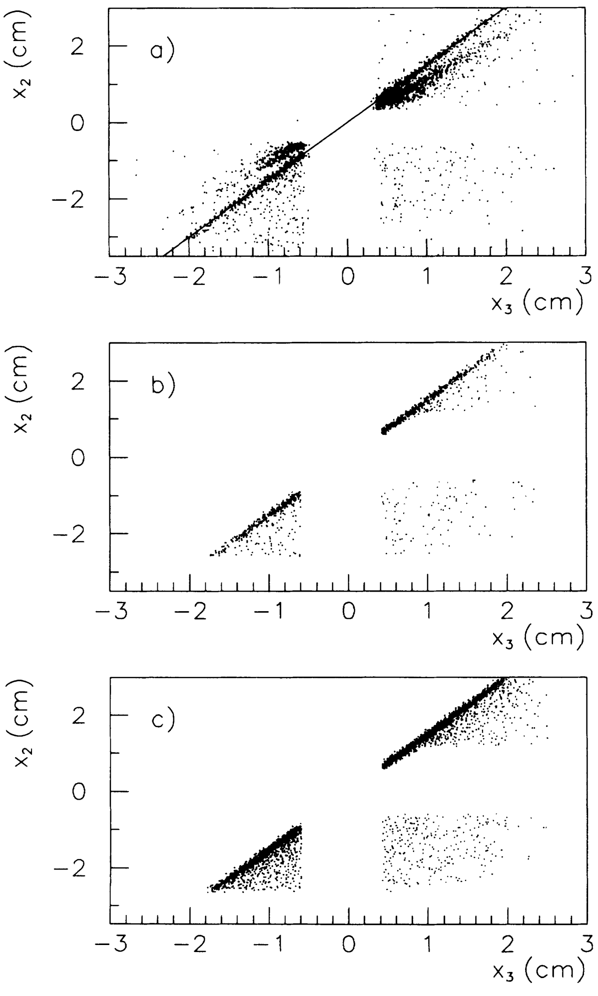

FIG. 4. Distribution of x_2 vs x_3 coordinates at $\sqrt{s} = 1800$. (a) All accepted events; (b) events which also pass all fiducial cuts listed in Table I; (c) simulated events.

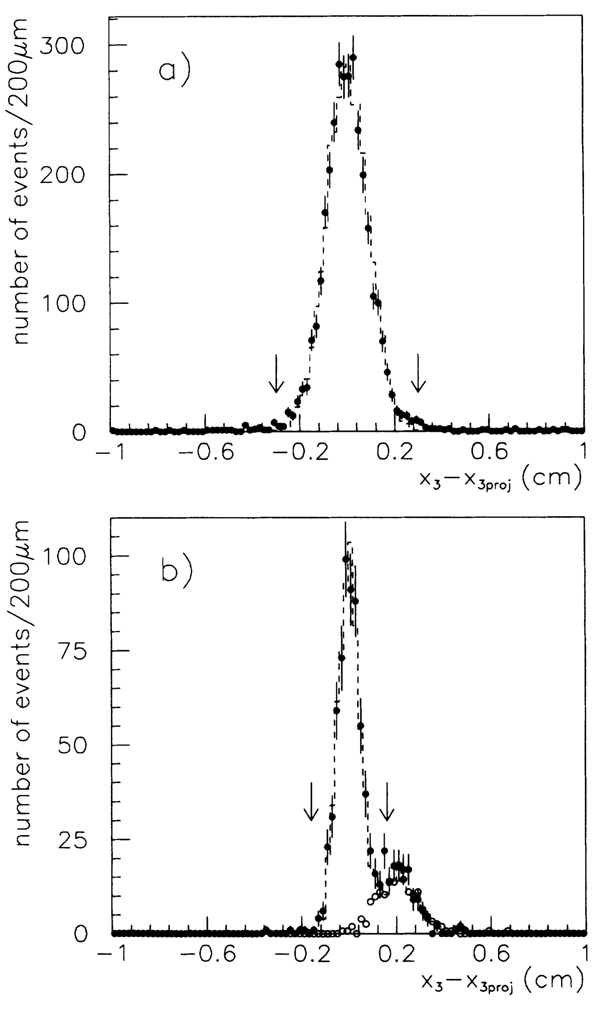

FIG. 5. (a) Distribution of (x_3-$x_{3\ \mathrm{proj}}$) at $\sqrt{s} = 546$, where x_3 is the x coordinate measured by $S3$ and $x_{3\ \mathrm{proj}}$ is the position in $S3$ evaluated by using $S1$, $S2$ and assuming $x = y = 0$ at $z = 0$. (●) Data; (– – –) simulation. The arrows mark the position of the FIDUCIAL CUT 2 (see text). (b) Distribution of (x_3-$x_{3\ \mathrm{proj}}$) at $\sqrt{s} = 1800$. (●) Data; (○) identified beam halo normalized to the data at (x_3-$x_{3\ \mathrm{proj}}$) ≥ 0.2 cm; (– – –) sum of the normalized halo and of the complementary amount of simulated events.

all fiducial cuts in this run was estimated to be $5 \pm 1\%$ in arm 0 and $1.8 \pm 0.4\%$ in all events. As shown, the data are accurately reproduced by the sum of the normalized background and a complementary amount of simulated events. The 5% background contamination was statistically removed by subtracting from the data the same amount of tagged halo events passing all cuts. The background in the second run at $\sqrt{s} = 1800$ was $\ll 1\%$.

Finally, events were rejected in which no vertex was found (VERTEX CUT). Figures 6 and 7 show vertex z distributions as reconstructed from data and simulation using the VTPC or FTF+$S5$ at $\sqrt{s} = 546$ and $\sqrt{s} = 1800$. One track is enough to reconstruct the vertex by determining its z position at which $x = y = 0$. The excellent agreement between data and simulation shows that the background contamination in our final sample is negligible.

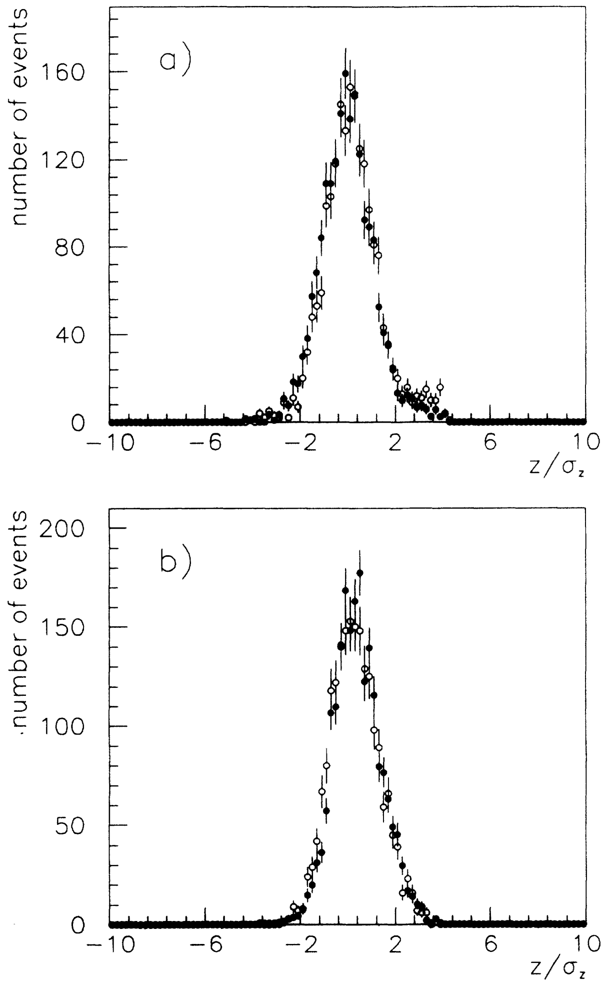

FIG. 6. Vertex z distributions measured at $\sqrt{s} = 546$. (a) Vertex measured by the VTPC in units of the spread σ_z of the interaction region ($\simeq \pm 30$ cm). The vertex reconstruction accuracy of the VTPC is $\simeq \pm 1$ cm. Data (•) and simulated events (∘) are filtered as described in Table I. (b) Vertex measured by the FTF and/or $S5$ detectors for events with no tracks in the VTPC in units of σ_z convoluted with the reconstruction error for each vertex ($\simeq \pm 10$ cm). (•) Data; (∘) simulation. The asymmetry in the z distributions for data and simulated events is caused by secondary interactions.

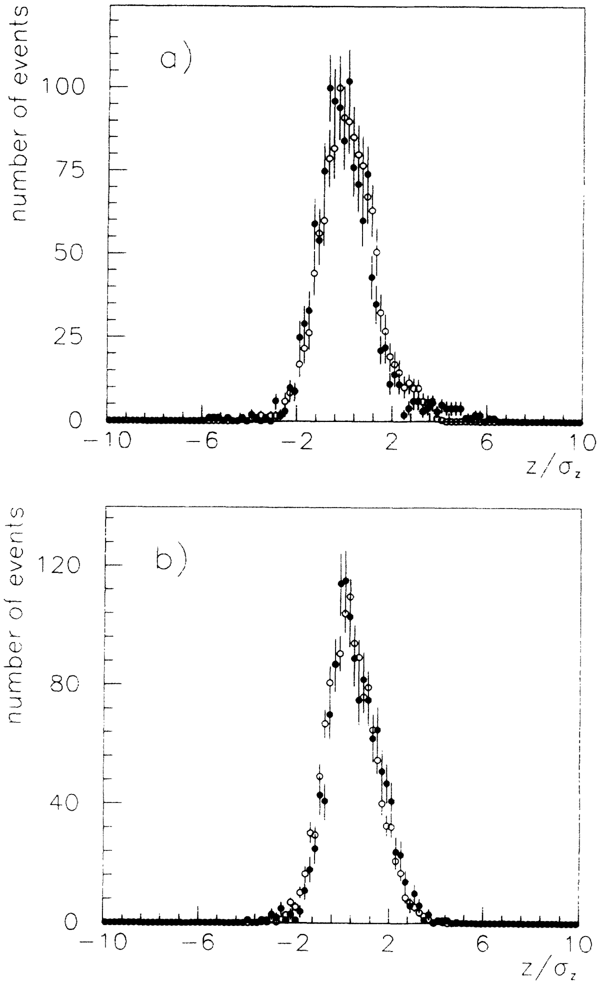

FIG. 7. Vertex z distributions at $\sqrt{s} = 1800$. (a) Vertex measured by the VTPC. (b) Vertex measured by the FTF and/or $S5$ detectors for events with no tracks in the VTPC. (•) Data; (∘) simulation.

Table I summarizes the event flow through all cuts and requirements leading to the final sample of events. Corrections for nuclear interactions in the spectrometer detectors, as measured in Ref. [1] and listed in Table I, were applied. The final numbers of events must be multiplied by the prescaling factor of the single diffractive trigger and by a factor of 2 to account for the dissociation of the antiproton, assumed to be the same as that of the proton.

IV. MONTE CARLO SIMULATION

The trigger and vertex finding efficiency, $E(M^2)$, was determined by simulation. Simulation details are given in Appendix B of Ref. [2]. In our simulation, single diffraction was generated in the mass range $1.4\ \mathrm{GeV}^2 < M^2 <$

0.15s with a distribution

$$d^2\sigma_{\rm SD}/dM^2dt = A\frac{b(M)}{M^2}e^{b(M)t} \qquad (1)$$

where $b(M) = \frac{2}{3}b_{\rm el}(1 + 0.04/\{[M(\text{GeV}) - \sqrt{2}]^2 + 0.02\})$ and $b_{\rm el}$ is the elastic slope [1].

The known resonances in the region $M^2 < 6$ GeV^2 were also generated. Their integrated cross section is equal to the integral of (1) below 6 GeV^2. For a given mass M (GeV) of the system X, the average generated total multiplicity is

$$n = 1.5[2 + 0.13\ln(M - m_p)^2 + 0.175\ln^2(M - m_p)^2]\ .$$

The multiplicity of each event was distributed according to the prescription given in Ref. [9]. For multiplicities larger than three, particle four-momenta were generated as described in Ref. [2]. Two- and three-body decays were generated according to exact phase space, assuming that the nucleon angular distribution in the rest frame of M is given by (1+cosθ^{*2}). Decay products were then boosted into the laboratory frame and tracked through the entire CDF detector [8], allowing for secondary decays, conversions and interactions in the beam pipe and all detector elements.

The resulting charged particle pseudorapidity distributions as seen by the VTPC,FTF, and $S5$ detectors are compared to the data at $\sqrt{s} = 546$ in Fig. 8. The same comparison at $\sqrt{s} = 1800$ is shown in Fig. 9. The agreement between data and simulation is impressive, especially in the trigger region at $\eta > 3.2$.

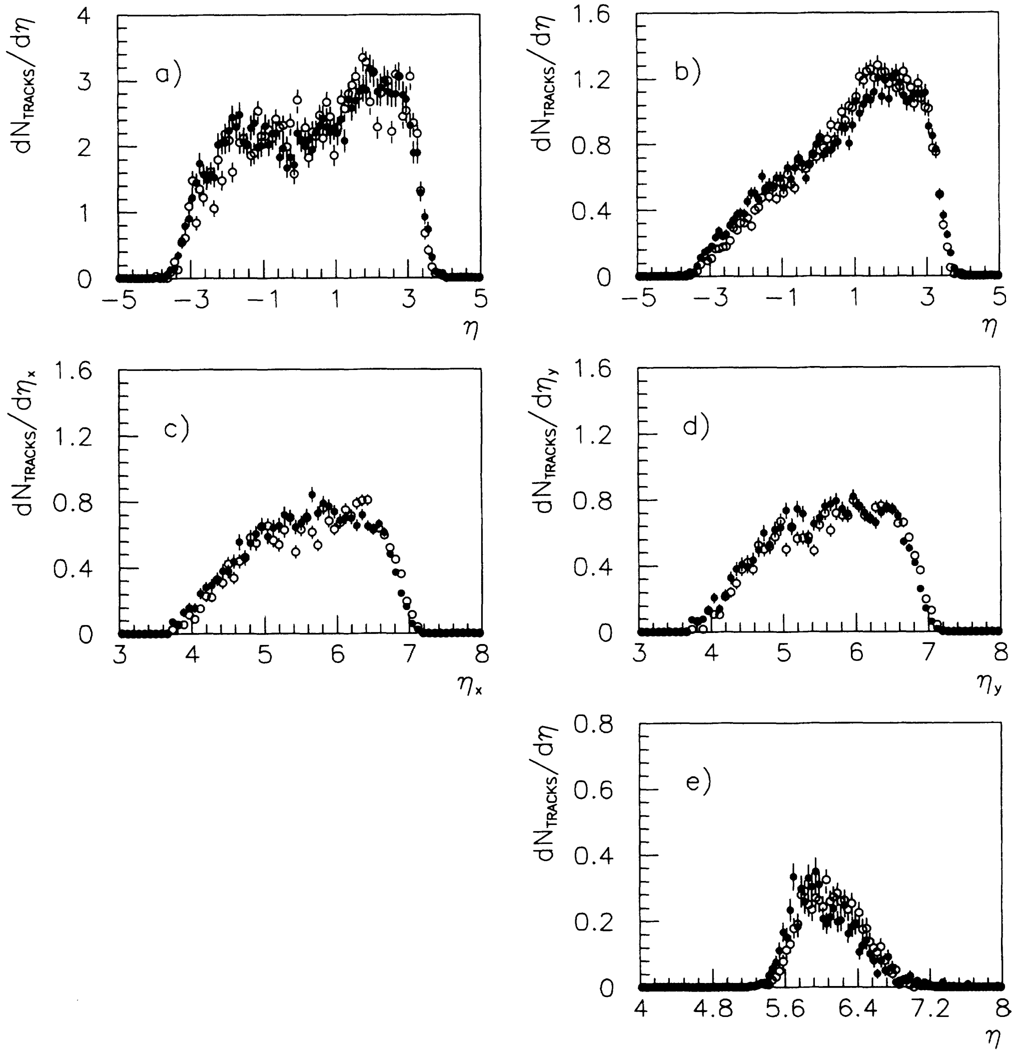

FIG. 8. Pseudorapidity distributions as measured by the different vertex detectors at $\sqrt{s} = 546$. Data (●) are not corrected for the detector acceptance. The simulation (○) is normalized to the total number of measured tracks. (a) η distribution of tracks detected by the VTPC for events with $x \le 0.95$. (b) η distribution of tracks detected by the VTPC for events with $x > 0.95$. (c), (d) η_x and η_y distributions measured by the FTF for all events. The angles θ_x and θ_y are measured independently and $\eta_{x(y)} = -\ln[\tan(\theta_{x(y)}/2)]$. (e) η distribution measured by $S5$ for all events.

The total number of measured tracks in all detectors compares well with the simulation at both energies (Fig. 10). The average number of tracks as a function of $(1-x)$ in the data and simulation is shown in Fig. 11. One may notice the partial agreement between data and simulation. Several effects contribute: the single diffraction differential cross section $d\sigma_{\rm SD}/dx$ used in the simulation is slightly different from the result of our fit to the data and, as discussed in Sec. VI, the data contain an appreciable nondiffractive contribution; in addition, the simulation accounts for secondary interactions, which appreciably increase the generated event multiplicity. For all these reasons, further work is needed to extract from the data accurate results on average multiplicities and angular distributions of diffractive events. However, for the purpose of estimating $E(M^2)$, the small differences between the observed and measured multiplicity distributions, particularly at large multiplicities, are not important.

Trigger and vertex-reconstruction inefficiencies on the diffractive cluster side are only due to 2- and 3-body decays, which, as mentioned above, are generated with exact phase space. For all $M^2 \leq 6$ GeV^2 (where 2- and 3-body decays dominate) the total efficiency is 73% and 36% at $\sqrt{s}=546$ and $\sqrt{s}=1800$, respectively. By changing the known ratio of the 2-body to 3-body decay fractions by a factor 2, the efficiency at both energies changes only by 1%. As diffractive masses become larger, the fraction of 2- and 3-body decay channels decreases and decay angles with respect to the proton increase, so that the efficiency $E(M^2)$ increases with M^2. The efficiency at our two energies is shown in Fig. 12 as a function of $(1-x)$ for $(1-x) \leq 0.0001$. The detector is fully

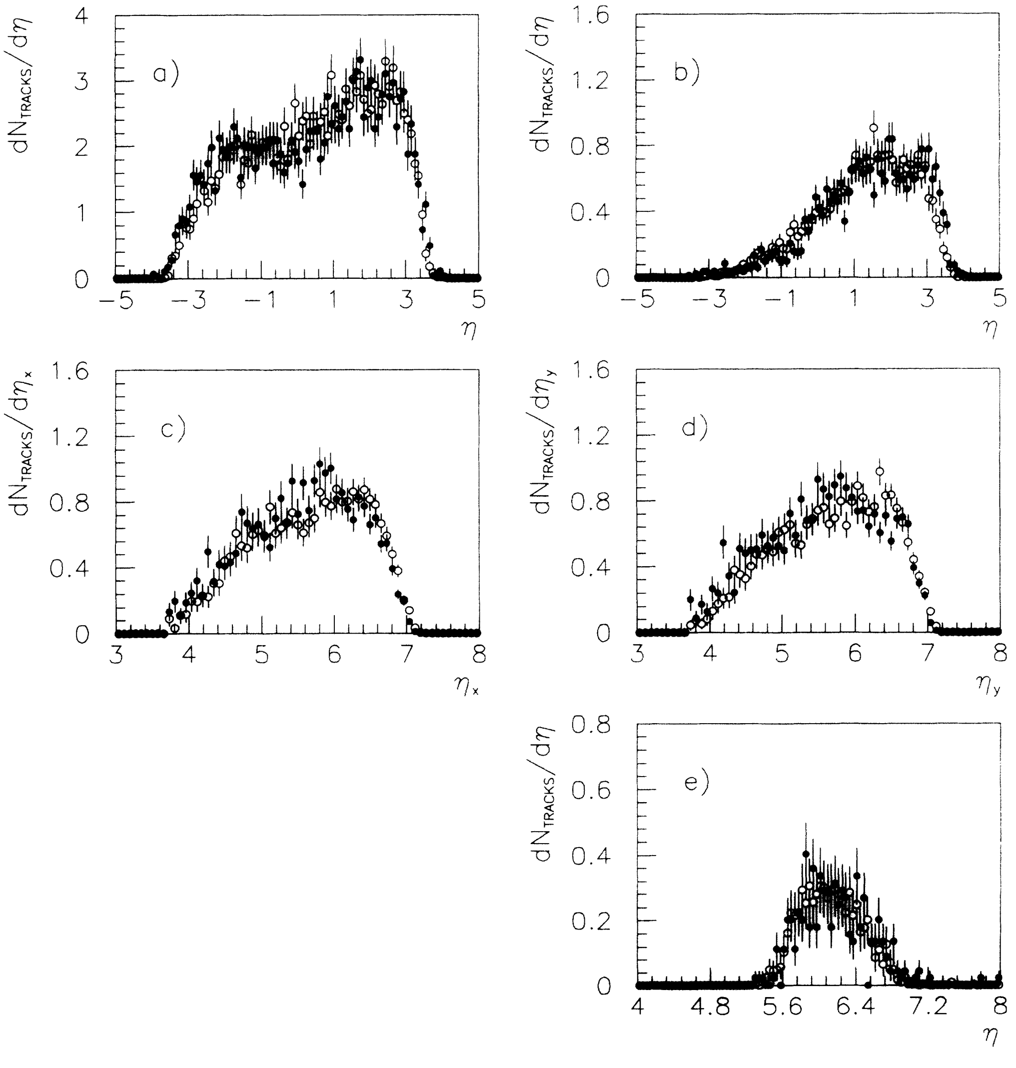

FIG. 9. Pseudorapidity distributions as measured by the different vertex detectors at $\sqrt{s}=1800$. Data (●) are not corrected for the detector acceptance. The simulation (○) is normalized to the total number of measured tracks. (a) η distribution of tracks detected by the VTPC for events with $x \leq 0.995$. (b) η distribution of tracks detected by the VTPC for events with $x > 0.995$. (c), (d) η_x and η_y distributions measured by the FTF for all events. (e) η distribution measured by $S5$ for all events.

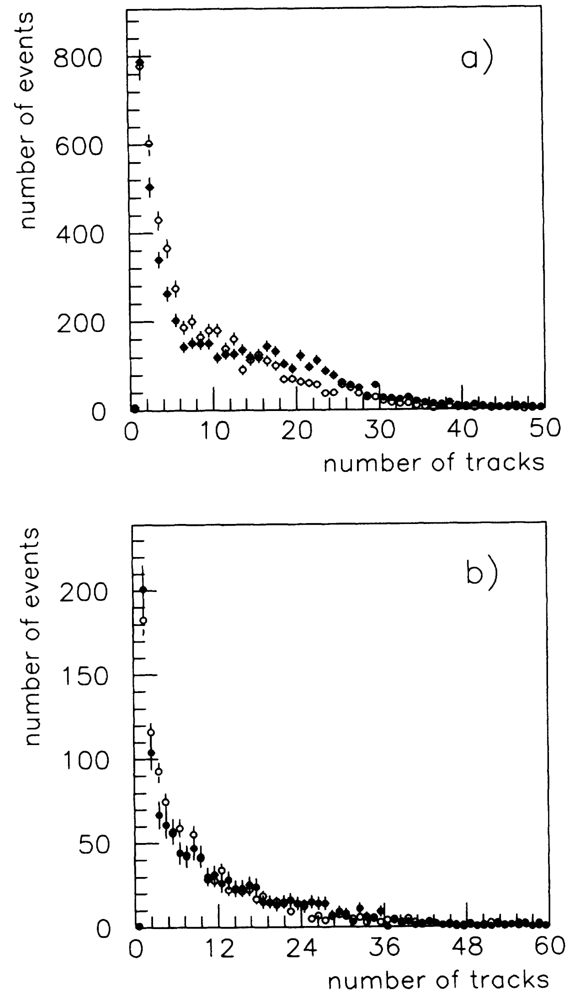

FIG. 10. Multiplicity distributions of tracks measured in all detectors. Data (•) and simulation (○) are compared at (a) $\sqrt{s} = 546$ and (b) $\sqrt{s} = 1800$.

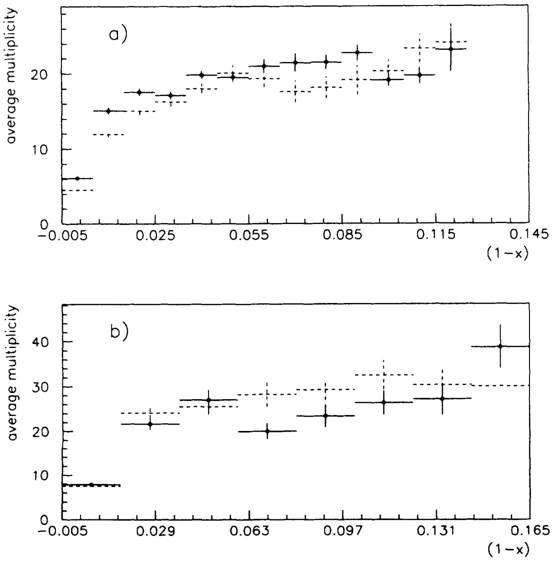

FIG. 11. Average number of tracks in all vertex detectors as a function of $(1-x)$. Data (•) and simulation (— — —) are compared at (a) $\sqrt{s} = 546$ and (b) $\sqrt{s} = 1800$.

efficient for events with $x < 0.998$; for $x > 0.998$, convoluting $E(x)$ with $d\sigma_{\rm SD}/dx$ from our best fit, we obtain an integrated efficiency

$$\int_{0.998}^{1}\frac{d\sigma_{\rm SD}}{dx}E(x)dx \Big/ \int_{0.998}^{1}\frac{d\sigma_{\rm SD}}{dx}dx \simeq 0.85(0.75)$$

$$\text{at } \sqrt{s} = 546(1800)\ \text{GeV}\ .$$

V. DATA FITTING

We fitted to our data the standard triple-Pomeron (PPP) Regge formula for single diffraction dissociation [5,10,11]:

$$sd^2\sigma_{\rm SD}/dM^2dt = G(t)(s/s_0)^{\alpha_p(0)-1}(s/M^2)^{2\alpha_p(t)-\alpha_p(0)}\ , \qquad (2)$$

where we lumped into $G(t)$ all four Regge couplings and the signature factors. Following tradition, we assumed a linear Pomeron trajectory $\alpha_p(t) = 1+\epsilon+\alpha' t$, treating ϵ as a free fit parameter and assuming $\alpha' = 0.25$ GeV^{-2} [1,5–7,12–14]. At each energy $G(t)(s/s_0)^{\epsilon}$ was parametrized as $G(0)(s/s_0)^{\epsilon}e^{b_0 t} = De^{b_0 t}$. Formula (2) can then be

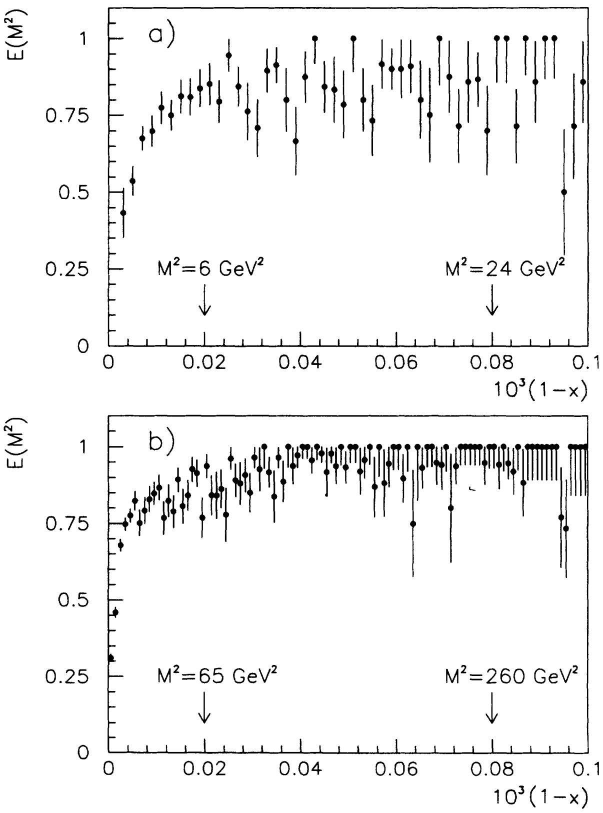

FIG. 12. Efficiency $E(M^2)$ for triggering on a diffractive cluster and reconstructing its vertex as a function of $1-x = M^2/s = (p_0 - p)/p_0$, where p is the recoil antiproton momentum. $E(M^2)$ is determined by our simulation at (a) $\sqrt{s} = 546$ and (b) $\sqrt{s} = 1800$.

TABLE II. Fit results.

	$\sqrt{s} = 546$ GeV	$\sqrt{s} = 1800$ GeV
$\int\int_{A(x,t)\geq 0.02} N_{\text{ev}}(M^2,t)dM^2dt$	4604±68	3671±85
$\int\int_{A(x,t)\geq 0.02} L\cdot\frac{d^2[\sigma_{\text{SD}}+\sigma_{\text{nd}}]}{dM^2dt}A(M^2,t)E(M^2)dM^2dt$	4597	3596
$L\sigma_{\text{SD}} = \int_{1.4\ \text{GeV}^2}^{0.15\ s} dM^2 \int_0^\infty L\cdot\frac{d^2\sigma_{\text{SD}}}{dM^2dt}dt$	162 836±7986	37 782±1770
$L\cdot\sigma_{\text{nd}} = \int_{1.4\ \text{GeV}^2}^{0.15\ s} dM^2 \int_0^\infty L\cdot\frac{d^2\sigma_{\text{nd}}}{dM^2dt}dt$	24 483±3926	10 276±1712
L (luminosity, mb^{-1})[a]	20 624±2.1%	3994±2.9%
σ_{SD} (mb)	7.89±0.33	9.46±0.44
$D = G(0)(s/s_0)^\epsilon$ (mb/GeV^2)	3.53±0.35	2.54±0.43
ϵ	0.121±0.011	0.103±0.017
b_0 (GeV^{-2})	7.7±0.6	4.2±0.5
σ_{nd} (mb)	1.2±0.2	2.6±0.4
I (mb/GeV^2)	537^{+498}_{-280}	162^{+160}_{-85}
b' (GeV^{-2})	10.2±1.5	7.3±1.0
γ	0.71±0.22	0.10±0.16

[a] Reference [2].

written as

$$s d^2\sigma_{\text{SD}}/dM^2dt = De^{[b_0+2\alpha'\ln(s/M^2)]t}(s/M^2)^{1+\epsilon} \quad (3)$$

In order to account for nondiffractive contributions at $x \geq 0.85$, we added to formula (3) the empirical term [7] (see Appendix C of Ref. [2])

$$d^2\sigma_{\text{nd}}/dxdt = I(1-x)^\gamma e^{b't}. \quad (4)$$

The sum (3)+(4), smeared by the detector resolution and the beam profile and multiplied by the acceptance $A(M^2,t)$, by the total integrated luminosity L and by $E(M^2)$, was fitted to the data using a maximum likelihood method to determine $G(0)(s/s_0)^\epsilon L = DL$, b_0, ϵ, IL, b', and γ.

VI. RESULTS

Fit results are listed in Table II and fit parameter correlation coefficients are given in Table III. Data and fits are compared in Figs. 13 and 14. In our fits, we assumed $\alpha' = 0.25$ GeV^{-2} in order to reduce the number of free parameters. A change in α' by ± 0.1 GeV^{-2} results in a change in σ_{SD} of only ±0.1%; at the same time, ϵ changes by $\delta\epsilon = \pm 0.011$ and b_0 by $\delta b_0 = \mp 1.5$ GeV^{-2}. These values $\delta\epsilon$ and δb_0 represent systematic errors to be added to the fit statistical errors for ϵ and b_0 at both energies. The negative systematic error $\delta\alpha' = -0.1$ GeV^{-2} is certainly an overestimate, but the resulting error $\delta\epsilon = -0.011$ is retained in order to cover the systematic error due to the fact that we cannot exclude an up to 15% contribution of a PPR triple-Regge term to the total single diffraction cross section (see Sec. VI E).

TABLE III. Fit parameter correlation matrix.

	b_0	I	b'	γ	ϵ
D	0.47	−0.74	0.08	0.66	−0.95
b_0		0.04	−0.3	−0.09	0.2
I			−0.17	−0.97	0.75
b'				0.33	−0.15
γ					0.69

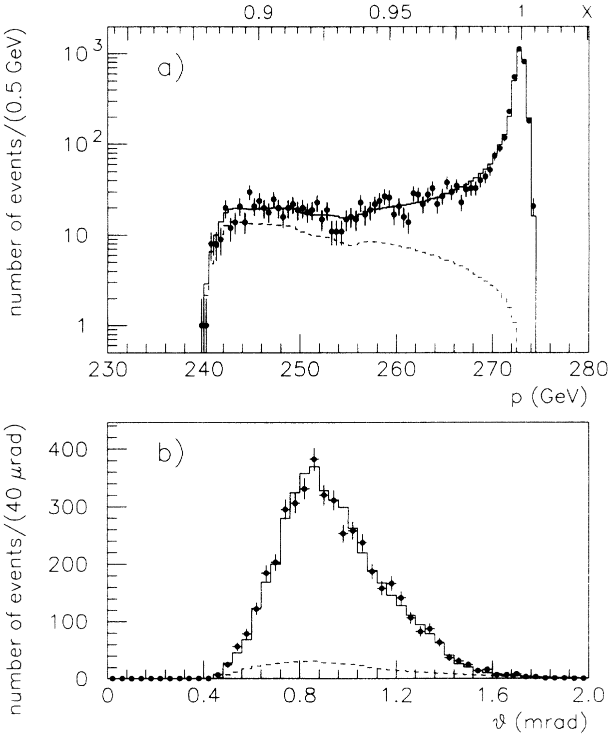

FIG. 13. (a) Recoil momentum distribution for all events at $\sqrt{s} = 546$. The data (●) are not corrected for the spectrometer acceptance A; the solid line represents our fit with form (3)+(4) (see Sec. V); the dashed line is the nondiffractive contribution (4). In our fit the data were arranged in a θ-p matrix with cells $\Delta\theta\Delta p = 40 \times 0.5$ μrad GeV. The momentum distribution shown was obtained by integrating over the spectrometer angular acceptance. (b) Recoil angular distribution for all events at $\sqrt{s} = 546$, after integrating over the spectrometer momentum acceptance. Data (●) are not corrected for the acceptance A; the solid line represents the fit (3)+(4); the dashed line is the nondiffractive contribution (4).

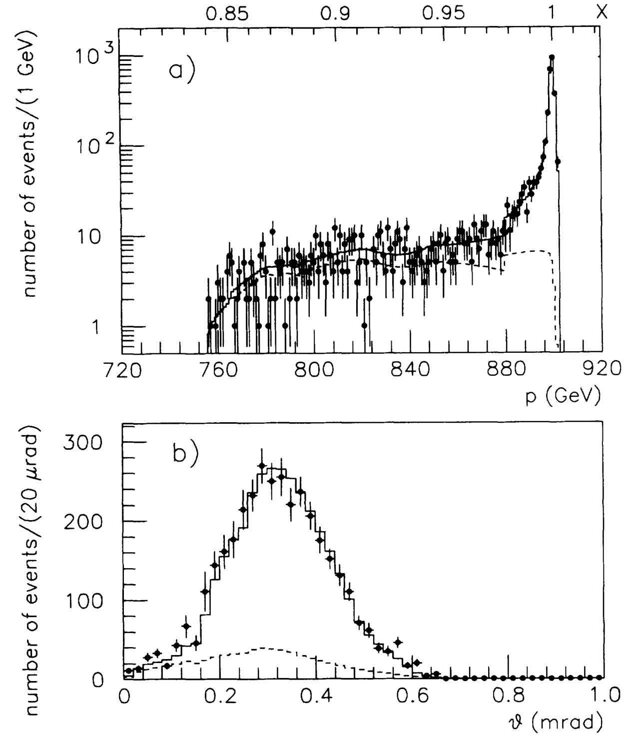

FIG. 14. (a) Recoil momentum and (b) production angle distributions at $\sqrt{s} = 1800$. At this energy, the data (●) were arranged in a mesh $\Delta\theta\Delta p = 20 \times 1.0$ μrad GeV. The solid line represents our fit (3)+(4); the dashed line is the nondiffractive contribution (4).

A. *t* dependence

The standard Regge form of the diffractive slope

$$b = b_0 + 0.5\ \text{GeV}^{-2}\ln(s/M^2) \qquad (5)$$

fits well our data at each energy. However, our fits yielded $b_0 = 7.7 \pm 0.6$ GeV^{-2} at $\sqrt{s} = 546$ and $b_0 = 4.2 \pm 0.5$ GeV^{-2} at $\sqrt{s} = 1800$. This difference in the b_0's may be a consequence of the fact that *low masses* ($M^2 \leq 6$ GeV^2), which represent a large fraction of the resolution-dominated diffractive peak at $x \simeq 1$ [Figs. 13(a) and 14(a)], have slopes steeper than those given by Eq. (5). At $M^2 \simeq 2$ GeV^2, the slopes derived from our fits are $b = 13.6$ and 11.3 GeV^{-2} at $\sqrt{s} = 546$ and 1800, respectively. These values are smaller than the elastic slopes $b_{el} = 15.35$ and 16.98 GeV^{-2} at the two energies, whereas at lower (fixed target) energies the *low mass* diffractive slopes were found to be larger than the elastic ones [15,16].

The region of $\pm 2\sigma_x$ around $x = 1$ contains 75% of all diffractive events at 546 and 78% at 1800 GeV. While the parameter ϵ is determined primarily by the remaining 25% (22%) of the events, the slope b_0 is determined mainly by the events in this $4\sigma_x$ region; of these events, 26% (13%) are estimated from our fit to be due to *low masses.* The difference in the b_0 values obtained at the two energies could be explained as the result of the different contribution of the *low masses* to the diffractive peak at $x \simeq 1$, if one assumed the average slope in the *low mass* region to be about 20 GeV^{-2}.

Since the D value in our fits is strongly correlated to b, the result for σ_{SD} is not very sensitive to the value of b_0. In fits where b_0 was varied by ± 2 GeV^{-2} or where the slope b was set to be 20 GeV^{-2} at *low masses* (see Sec. VI D), the result for σ_{SD} did not change by more than 1%.

B. M^2 dependence

The parameter ϵ, which measures the deviation of the differential cross section $d\sigma_{\text{SD}}/dM^2$ from $1/M^2$ dependence, was determined to be $\epsilon = 0.121 \pm 0.011$ at $\sqrt{s} = 546$ and $\epsilon = 0.103 \pm 0.017$ at $\sqrt{s} = 1800$. Theoretically, $1 + \epsilon$ can be interpreted as the intercept of a supercritical Pomeron, assuming that only the triple-Pomeron diagram contributes to diffraction dissociation (see also Sec. VI E) and neglecting screening effects. In terms of single Pomeron exchange, the $\bar{p}p$ total cross section σ_T behaves at high energies as $s^{\alpha_P(0)-1} = s^{\epsilon}$. From our measurements of σ_T at $\sqrt{s} = 546$ and $\sqrt{s} = 1800$ [2] we derive $\epsilon = 0.112 \pm 0.013$. This ϵ value is in good agreement with the average ϵ value 0.116 ± 0.010(stat) ± 0.011 (syst) obtained from the single diffraction M^2 dependence at our two energies.

C. *s* dependence

According to Eq. (3), the total diffractive cross section is given by

$$\sigma_{\text{SD}} = G(0)(s/s_0)^{\epsilon}s^{\epsilon}\int_{1.4\ \text{GeV}^2}^{0.15s}\frac{M^{-2(1+\epsilon)}}{b_0 + 0.5\ln(s/M^2)}dM^2 \ . \qquad (6)$$

Using $\epsilon = 0.112 \pm 0.013$ (from the rise of σ_T) and $b_0 = 6.0$ GeV^{-2} (average over our two energies), the value of $\sigma_{\text{SD}} = 7.89 \pm 0.33$ mb measured at $\sqrt{s} = 546$ extrapolates to $\sigma_{\text{SD}} = 13.9 \pm 0.9$ mb at $\sqrt{s} = 1800$, where we measure $\sigma_{\text{SD}} = 9.46 \pm 0.44$ mb. The ratio of the measured σ_{SD} at $\sqrt{s} = 1800$ to that obtained by extrapolation from $\sqrt{s} = 546$ is 0.68 ± 0.05, clearly indicating that large screening corrections have to be introduced in order to save the traditional supercritical Pomeron model.

Direct comparison of our results with experiments at lower energies is made difficult by the fact that the data in these experiments were not fitted with exactly the same function as ours. To compare our results to lower energy data, we fitted the form (3)+(4) to published data at $\sqrt{s} = 20$ GeV [17], supplemented by points measured in the region $x \leq 0.95$ at $\sqrt{s} = 23.5$ GeV [18]. Since t distributions as a function of M^2 are not available from these experiments, we used in the fits $b = 4.5 + 0.5\ln(s/M^2)$ GeV^{-2} for single diffraction and $b' = 6.5$ GeV^{-2} for the nondiffractive contribution, consistent with the slopes given in [17,18] and with other measurements at the ISR [19].

Our fit to the low energy data is shown in Fig. 15. The fit results are listed below.

$\sigma_{\rm SD}$(mb)	D (mb/GeV^2)	ϵ	$\sigma_{\rm nd}$ (mb)	I (mb/GeV^2)	γ
4.9 ± 0.3	4.5 ± 2.4	0.20 ± 0.12	1.7 ± 0.3	642 ± 289	0.83 ± 0.27

The cross section values listed above are for $x \geq 0.85$. We estimate that, due to the uncertainty in the slopes [19], a 10% systematic error should be attached to these cross sections.

The measured $\sigma_{\rm SD} = 4.9 \pm 0.55$ mb at $\sqrt{s} = 20$ GeV is 4.5 times larger than the value $\sigma_{\rm SD} = 1.1 \pm 0.17$ mb obtained by extrapolating our measured value at $\sqrt{s} = 546$ down to $\sqrt{s} = 20$ using Eq. (6). It is interesting to note that the factor 4.5 is almost entirely due to the term $s^{2\epsilon}$ in Eq. (6).

According to the Good-Walker quantum-mechanical picture [3], the single diffraction dissociation cross section is expected to vanish asymptotically as the c.m.s. energy increases and the colliding system becomes black. From $\sqrt{s} = 20$ to $\sqrt{s} = 1800$ GeV, the $\bar{p}p$ system becomes more opaque, since the ratio $\sigma_{\rm el}/\sigma_T$ increases from 0.17 ± 0.01 to 0.246 ± 0.004 [2]. Theoretical models [20,21], which incorporate the expansion of the effective interaction area and the increasing opacity of the collision system within the general geometric picture, predict that, with increasing s, the single diffraction cross section reaches a broad maximum and then falls as the collision system blackens. Other theoretical approaches [22–24], which describe single diffraction dissociation as a multi-Pomeron exchange with the eikonal formalism, also predict a rather flat s dependence of $\sigma_{\rm SD}$ while breaking the (s/M^2) scaling of $s d^2\sigma_{\rm SD}/dM^2 dt$. A useful representation of Eq. (6) for testing such models is

$$\sigma_{\rm SD} = K(s/s_0)^\delta \int_{1.4\ {\rm GeV}^2}^{0.15\ s} \frac{(M/m_0)^{-2(1+\epsilon)}}{b_0 + 0.5\ln(s/M^2)} dM^2 \ . \quad (7)$$

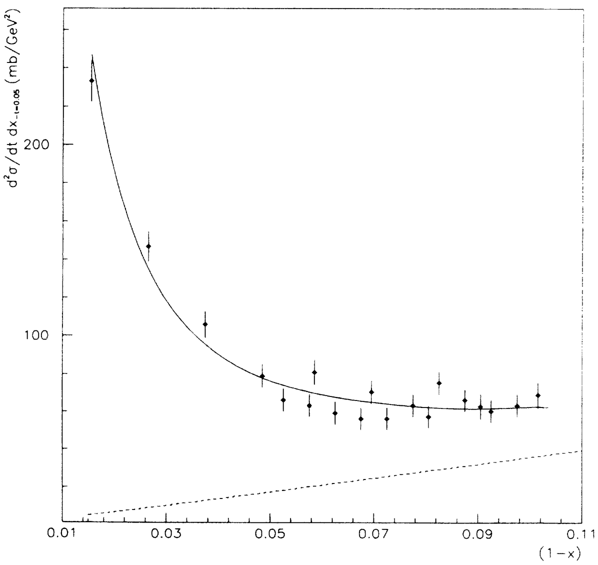

FIG. 15. $(1-x)$ distribution of data at $\sqrt{s} = 20$ GeV from [17,18]. The data (●) are at $-t = 0.05$. The solid line is the fitted form (3)+(4); the dashed line is the nondiffractive contribution (4).

Treating δ as a free parameter, we determined its value from a simultaneous fit to the diffractive cross sections $\sigma_{\rm SD}$ at $\sqrt{s} = 20$, 546, and 1800 GeV. Using the average value $b_0 = 5.4$ GeV^{-2} at all three energies and assuming a common $\epsilon = 0.116 \pm 0.010$, we obtained $\delta = 0.030 \pm 0.016$; by fitting $\sigma_{\rm SD}$ only at $\sqrt{s} = 546$ and 1800 GeV, we obtained $\delta = 0.068 \pm 0.026$.

D. Comparison with other experiments

At $\sqrt{s} = 546$, our total inelastic cross section in the region $x \geq 0.85$ is 9.09 ± 0.25 mb, of which $\sigma_{\rm SD}$ accounts for 7.89 ± 0.33 mb. At the same energy, the UA4 experiment [25] obtained the value $\sigma_{\rm SD} = 9.4 \pm 0.7$ mb for $x \geq 0.95$, corresponding to $\sigma_{\rm SD} = 10.4 \pm 0.8$ mb for $x \geq 0.85$.

The discrepancy between the two results for $\sigma_{\rm SD}$ can be understood in terms of the way the data were fitted in the two experiments. Motivated by lower energy experiments [15], UA4 fitted to the data the expression

$$d^2\sigma_{\rm SD}/dt\,dM^2 = \frac{D}{M^2} e^{b_0 t} \ , \quad (8)$$

which is the same as (3) when $\epsilon = 0$ and $\alpha' = 0$. The parameter D was allowed to be different in the resonance region of $M^2 < 16$ GeV^2, and nondiffractive contributions, which account for most of the discrepancy, were incorporated into $\sigma_{\rm SD}$. The fit yielded $b_0 = 8.0 \pm 0.1$ GeV^{-2} and a discontinuity in the mass

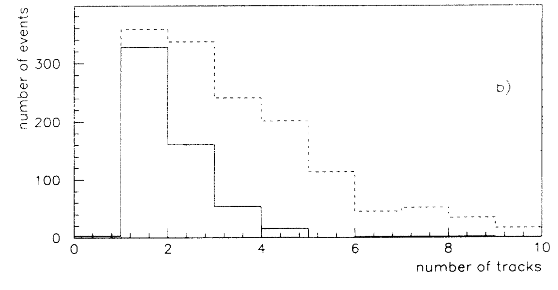

FIG. 16. Distribution of the number of tracks at $\sqrt{s} = 546$. (a) Tracks measured by the FTF+$S5$ detectors for events with $x \geq 0.996$ and no tracks in the VTPC. (●) Data; (− − −) best fit using the shapes in (b). (b) Tracks measured by the FTF+$S5$ detectors for simulated events with $x \geq 0.996$, no tracks in the VTPC and $M^2 \leq 6$ GeV^2 (solid line) or $M^2 > 6$ GeV^2 (dashed line).

spectrum: $D/b_0 = 0.93 \pm 0.09$ mb for $M^2 > 16$ GeV^2 (corresponding to $\sigma_{\mathrm{SD}[M^2>16\ \mathrm{GeV}^2]} = 7.4 \pm 0.5$ mb) and $D/b_0 = 1.23 \pm 0.26$ mb in the region $M^2 \leq 16$ GeV^2 (corresponding to $\sigma_{\mathrm{SD}[M^2\leq 16\ \mathrm{GeV}^2]} = 3.0 \pm 0.6$ mb).

Following the same approach, we also fitted (8) to our data, allowing D and b_0 to be different at $M^2 < 16$ GeV^2. However, because of our good mass resolution in the high mass region compared to that of UA4, in order to obtain a reasonable fit at all masses we were forced to add to (8) the term (4), which accounts for nondiffractive contributions. This fit yielded a total integrated cross section in the mass region 1.4 GeV^2 < M^2 < $0.15s$ of 11.3 ± 0.5 mb and, as expected, a larger discontinuity in the mass spectrum. The results of the fit are listed below.

σ_{SD} (mb)	$\sigma_{\mathrm{SD}[M^2>16\ \mathrm{GeV}^2]}$ (mb)	$\sigma_{\mathrm{SD}[M^2\leq 16\ \mathrm{GeV}^2]}$ (mb)	σ_{nd} (mb)
10.3 ± 0.4	5.4 ± 0.3	4.9 ± 0.3	1.0 ± 0.6

$b_{0[M^2>16\ \mathrm{GeV}^2]}$ (GeV^{-2})	$b_{0[M^2\leq 16\ \mathrm{GeV}^2]}$ (GeV^{-2})	b'(GeV^{-2})	γ
7.4 ± 1.0	20.0 ± 3.0	12.0 ± 2.0	1.0 ± 0.2

D/b_0 (mb)	D/b_0 (mb)
0.72 ± 0.05	1.88 ± 0.10

The reason for obtaining a larger single diffraction cross section by using form (8) in place of (3) can be traced to the steeper than $1/M^2$ dependence of the differential cross section in the data, coupled to the fact that the diffractive peak in the low mass region ($x \simeq 1$) is smeared by resolution. Fitting the large mass data with (8) forces more events to be considered as belonging to the *low mass* ($M^2 \leq 6$ GeV^2) region, where the efficiency $E(M^2)$ is low (see Fig. 12). The efficiency correction, which is 1.37 averaging over all *low masses*, produces an artificially higher cross section in this mass region. A quantitative argument that definitely favors the form (3)+(4) over (8)+(4) is based upon the observed track multiplicity distributions. At $\sqrt{s} = 546$, within the region $(1-x) \leq 0.004$, we expect 26% or 48% of the events to be in the *low mass* region depending on whether we use our fit (3)+(4) or the fit (8)+(4). Since lower masses have lower multiplicities, the fraction of *low mass* events in the region $(1-x) \leq 0.004, F_{l-m}$, can be extracted from the measured track multiplicity distribution. Figure 16(a) shows the multiplicity distribution of tracks observed in the FTF and/or $S5$ for events with $(1-x) \leq 0.004$ and no tracks in the VTPC. The multiplicity distribution for simulated events in the region of $(1-x) \leq 0.004$ with no tracks in the VTPC is shown in Fig. 16(b) for masses below and above 6 GeV^2. By fitting the two simulated shapes to the data, F_{l-m} is estimated to be 23 ± 3%.

An additional way of determining F_{l-m} is offered by the observation that, according to our simulation, *low mass* events never have tracks in the VTPC. On the contrary, 28% of the simulated events with $M^2 > 6$ GeV^2 and $(1-x) \leq 0.004$ have tracks in the VTPC. In the data, out of 2723 events at $(1-x) \leq 0.004$, 545 events have one or more tracks in the VTPC, reflecting a *low mass* contribution of 28 ± 3.5%. The average of the two numbers, the first one derived by fitting the multiplicity distribution and the second by using the pseudorapidity distribution, is $F_{l-m} = 25 \pm 3$%, in agreement with the value 26% from our fit (3)+(4).

E. Estimate of a possible PPR contribution

The form (3)+(4), based on the PPP triple-Regge term with a supercritical Pomeron and an empirical nondiffractive inelastic contribution, provides a good fit to our data and allows a precise integration of the single diffraction cross section. We have also investigated the effect of adding a PPR term [11], which is given by

$$\begin{aligned} s\frac{d^2\sigma_{\mathrm{PPR}}}{dM^2dt} &= G_{\mathrm{PPR}}(t)\left(\frac{s}{s_0}\right)^{\alpha_R(0)-1}\left(\frac{s}{M^2}\right)^{2\alpha_P(t)-\alpha_R(0)} \\ &= G_{\mathrm{PPR}}(0)\left(\frac{s}{s_0}\right)^{-0.5} e^{[b_1+2\alpha'\ln(s/M^2)]t}\left(\frac{s}{M^2}\right)^{1.5+2\epsilon} , \end{aligned} \tag{9}$$

where $\alpha_R(0) = 0.5$. This term has a steeper mass dependence than the PPP term and therefore its addition reduces the ϵ value in the PPP term. Since the PPR contribution is contained mainly within the resolution-dominated diffractive peak ($x > 0.996$ at $\sqrt{s} = 546$), this type of fit cannot determine unambiguously both ϵ and $G_{\mathrm{PPR}}(0)$. However, a sizable PPR term results in a larger fraction F_{l-m} of *low mass* events and this fact can be used to estimate its contribution. At $\sqrt{s} = 546$, fits were made to the data for several values of ϵ between 0 and 0.132; in every fit, $G_{\mathrm{PPR}}(0)$ was a free fit parameter and b_1 was assumed to be the same as b_0 in the PPP term. For increasing ϵ values, the data are always fitted well with a decreasing PPR contribution and a conse-

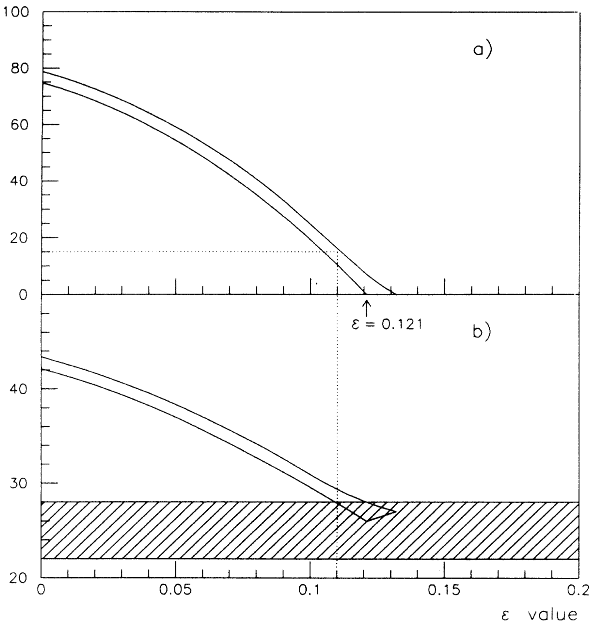

FIG. 17. Result of fits to the recoil antiproton $\frac{d^2\sigma}{dM^2dt}$ distribution at $\sqrt{s} = 546$ GeV with a PPR term added to the PPP triple-Regge term and the nondiffractive inelastic contribution. (a) The solid lines indicate the 1σ bounds of the fraction of $\sigma_{\rm SD}$ attributed to the PPR term by fits to the data as a function of the ϵ-value. (b) The solid lines indicate the 1σ bounds of the fraction F_{l-m} of *low mass* events in the region $(1-x) < 0.004$ as derived from the fits in (a). The hatched area indicates the 1σ bounds of F_{l-m} derived from the analysis of the products of the proton dissociation. The dotted line indicates the minimum allowed value of ϵ and the corresponding maximum allowed value of $F_{\rm PPR}$.

quently increasing PPP term. Figure 17(a) shows the fraction of $\sigma_{\rm SD}$ attributed by our fit to the PPR term as a function of the ϵ-value. Figure 17(b) shows the ϵ dependence of the fraction F_{l-m} calculated from the fit results shown in Fig. 17(a). The hatched area in Fig. 17(b) marks the 25 ± 3% region allowed for F_{l-m} from the previously described analysis of the tracks from the proton dissociation. A contribution of a PPR term as large as $0.15\sigma_{\rm SD}$ is compatible with our data; a consequent reduction $\delta\epsilon = -0.011$ is derived.

VII. CONCLUSIONS

We have measured the single diffraction dissociation differential cross section for $\bar{p}p \to \bar{p}X$ at $\sqrt{s} = 546$ and 1800 GeV and compared our results to theoretical expectations based on triple-Pomeron Regge model with a linear Pomeron trajectory $\alpha(t) = 1 + \epsilon + \alpha' t$. The measured t distributions are consistent with a slope $b = b_0 + 2\alpha'\ln(s/M^2)$, using the values $\alpha' = 0.25$ GeV^{-2} and $b_0 = 6.0 \pm 1.8$ GeV^{-2}. Fitting the measured M^2 distribution with the form $1/(M^2)^{1+\epsilon}$, we obtained $\epsilon = 0.121 \pm 0.011({\rm stat}) \pm 0.011({\rm syst})$ $(0.103 \pm 0.017 \pm 0.011)$ at $\sqrt{s} = 546$ (1800) GeV. These ϵ values are in good agreement with the value of $\epsilon = 0.112 \pm 0.013$ obtained from the rise of the $\bar{p}p$ total cross section in this energy region, as expected in the model. A contribution of a PPR term larger than 15% $\sigma_{\rm SD}$ is excluded by our data. The measured s dependence of the single diffraction total cross section shows a $s^{2(0.015\pm0.008)}$ behavior in place of the $s^{2\epsilon}$ term in the model, strongly indicating the need for screening corrections.

ACKNOWLEDGMENTS

We thank the Fermilab Accelerator Division for the construction and operation of the Tevatron and of the Antiproton Source. We wish to thank the Fermilab Computer Division, the technical staff of CDF, and the collaborating Institutions for their contribution to the construction and operation of CDF. The dedicated effort of the many technicians and engineers at Frascati and Rockefeller, who contributed to the design, construction and installation of the spectrometer and of the forward tracking vertex detectors, is warmly acknowledged; we especially thank M. Biagioli, G. Bisogni, A. Ceccarelli, M. DiVirgilio, G. Fontana, R. Heidecker, D. Humbert, E. Iacuessa, P. Locchi, A. Rutili, G. Sensolini, D. Scepanovich, and M. Troiani. We are grateful to G. Tonelli and E. Focardi who led the construction of our silicon detectors. A very special thanks is due to our friends and colleagues R. Castaldi, C. Vannini, and G. Sanguinetti, who made available to us most of the UA4 drift chambers (FTF and FTB), patiently introduced us to their reconstruction code, and over several years have been helpful through many useful discussions. This work was supported by the Department of Energy, the National Science Foundation, the Istituto Nazionale di Fisica Nucleare, and the Ministry of Science, Culture and Education of Japan.

---

[1] CDF Collaboration, F. Abe *et al.*, preceding paper, Phys. Rev. D **50**, 5518 (1994).
[2] CDF Collaboration, F. Abe *et al.*, following paper, Phys. Rev. D **50**, 5550 (1994).
[3] M. L. Good and W. D. Walker, Phys. Rev. **120**, 1857 (1960).
[4] P. D. B. Collins, *An Introduction to Regge Theory and High-Energy Physics* (Cambridge University Press, Cambridge, England, 1977).
[5] D. P. Roy and R. G. Roberts, Nucl. Phys. **B77**, 240 (1974).
[6] G. Alberi and G. Goggi, Phys. Rep. **74**, 1 (1981).
[7] K. Goulianos, Phys. Rep. **101**, 169 (1983).
[8] CDF Collaboration, Nucl. Instrum. Methods **A271**, 387 (1988); CDF Collaboration, Nucl. Instrum. Methods **A268**, 75 (1988).
[9] K. Goulianos, Phys. Lett. B **193**, 151 (1987).
[10] L. Angelini, L. Nitti, M. Pellicoro, and G. Preparata,

Phys. Rev. D **41**, 2081 (1990).
[11] R. D. Field and G. C. Fox, Nucl. Phys. **B80**, 367 (1974).
[12] A. Donnachie and P. V. Landshoff, Phys. Lett. **123B**, 345 (1983).
[13] P. D. B. Collins and F. Gault, Phys. Lett. **112B**, 255 (1982).
[14] A. Capella, J. Tran Thanh Van, and J. Kwiecinski, Phys. Rev. Lett. **58**, 2015 (1987).
[15] Y. Akimov *et al.*, Phys. Rev. D **14**, 3148 (1976).
[16] Y. Akimov *et al.*, Phys. Rev. Lett. **35**, 763 (1975).
[17] R. L. Cool, K. Goulianos, S. L. Segler, H. Sticker, and S. N. White, Phys. Rev. Lett. **47**, 701 (1981).
[18] J. C. Armitage *et al.*, Nucl. Phys. **B194**, 365 (1982).
[19] M. G. Albrow *et al.*, Nucl. Phys. **B108**, 1 (1976).
[20] S. Barshay and H. Kondo, Phys. Lett. B **177**, 441 (1986).
[21] S. Barshay, P. Heiliger, and D. Rein, Z. Phys. C **52**, 77 (1992).
[22] E. Gotsman, E. M. Levin, and U. Maor, Phys. Rev. D **49**, 4321 (1994).
[23] R. Engel, F. W. Bopp, D. Pattermann, and J. Ranft, Phys. Rev. D **46**, 5192 (1992).
[24] P. Aurenche, A. Cappella, J. Kwiecinski, M. Maire, J. Ranft, and J. Tran Thanh Van, Phys. Rev. D **45**, 92 (1992).
[25] UA4 Collaboration, D. Bernard *et al.*, Phys. Lett. B **186**, 227 (1987).

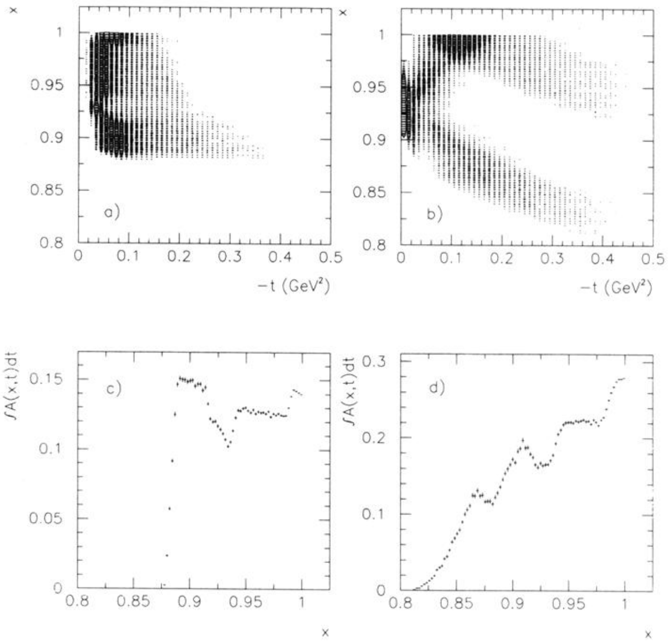

FIG. 2. Spectrometer acceptance $A(x,t)$ at (a) $\sqrt{s} = 546$ and (b) $\sqrt{s} = 1800$. Integrated acceptance $\int_0^{0.5} A(x,|t|)d|t|$ at (c) $\sqrt{s} = 546$ and (d) $\sqrt{s} = 1800$.

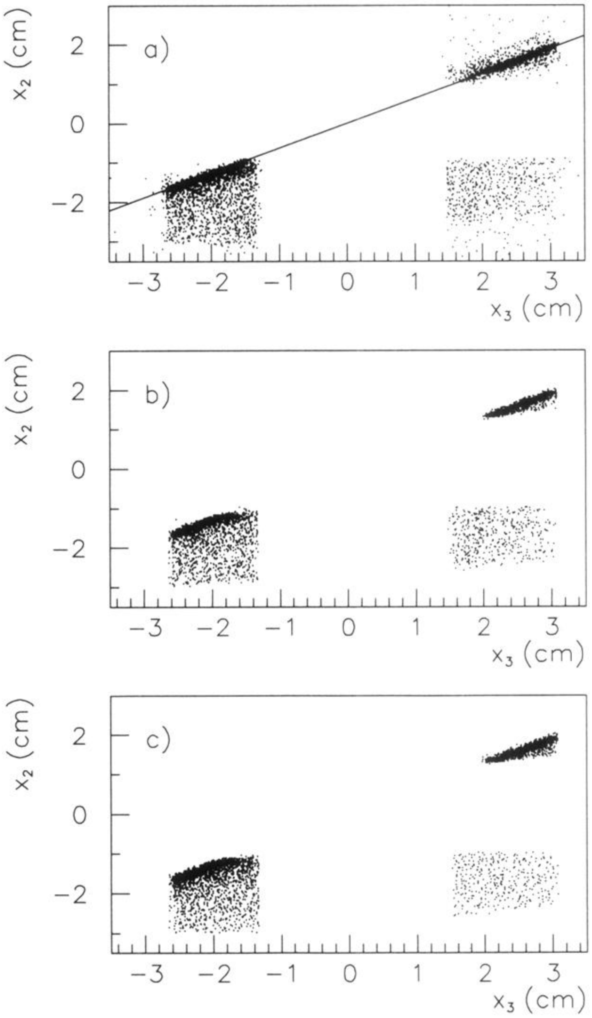

FIG. 3. Distribution of antiproton x_2 vs x_3 coordinates at $\sqrt{s}$ = 546 (the $S2$ and $S3$ detectors are separated by a string of dipole magnets). (a) All accepted events; (b) events which also pass all fiducial cuts listed in Table I; (c) simulated events.

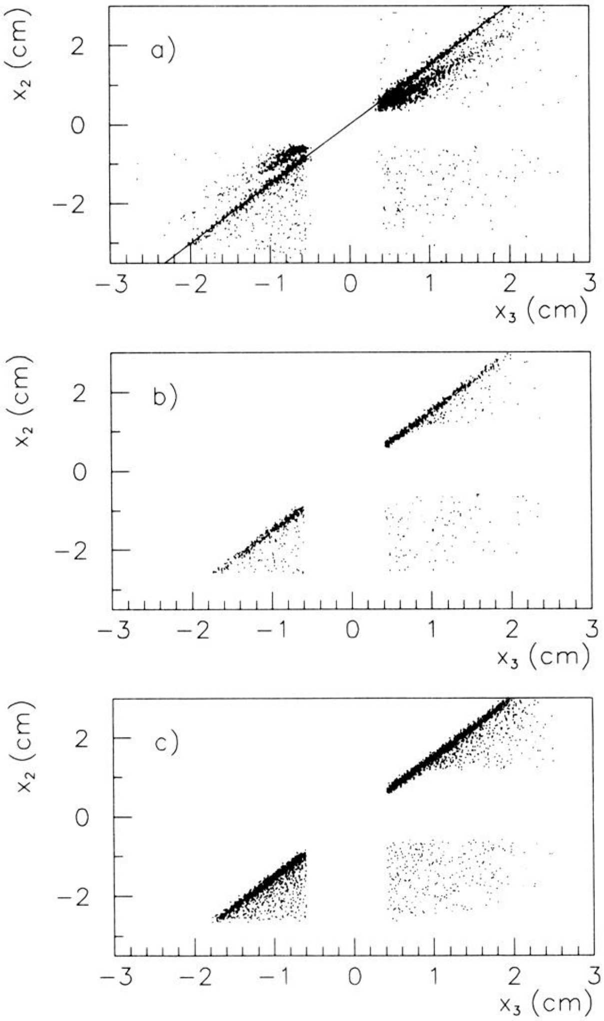

FIG. 4. Distribution of x_2 vs x_3 coordinates at $\sqrt{s} = 1800$. (a) All accepted events; (b) events which also pass all fiducial cuts listed in Table I; (c) simulated events.